

Tunable Competing Electronic Orders in Double Quantum Spin Hall Superlattices

Yi-Chun Hung,^{1,2,*} Chen-Hsuan Hsu,³ and Arun Bansil^{1,2,†}

¹*Department of Physics, Northeastern University, Boston, Massachusetts 02115, USA*

²*Quantum Materials and Sensing Institute, Northeastern University, Burlington, Massachusetts 01803, USA*

³*Institute of Physics, Academia Sinica, Taipei 115201, Taiwan*

Competing superconducting (SC) and density-wave orders are of key importance in generating unconventional superconductivity and emergent electronic responses. Quasi-one-dimensional models provide insight into these competing orders and suggest higher-dimensional realizations through coupled-wire constructions, but analysis of such systems remains limited. Recent studies suggest that double helical edge states (DHESs) in double quantum spin Hall insulators (DQSHIs) form a two-channel Luttinger liquid that exhibits SC and spin density wave (SDW) phases and their π -junction analogs. Here, we analyze weakly coupled DHESs from the surface of a periodically stacked layered structure consisting of DQSHIs and dielectrics, where inter-edge interactions approximately develop a tunable helical sliding Luttinger liquid (HSLL) order. Using a renormalization-group analysis, we construct phase diagrams and identify a regime of HSLL parameters that favor competing two-dimensional π -SC and π -SDW orders. We identify parameter regimes where the competing orders could be realized experimentally in nanoscale devices. Our study suggests a promising materials platform for exploring tunable π -SC and π -SDW orders in double quantum spin Hall superlattices.

I. INTRODUCTION

Strongly correlated electronic systems are usually characterized by complex phase diagrams with multiple competing orders. Examples include high-temperature superconductors [1, 2] and kagome materials which exhibit complex interplay of superconducting (SC), charge density wave (CDW) and other orders [3–10]. The coexistence or competition of SC and spin density wave (SDW) phases is another hallmark of unconventional superconductivity in iron-based compounds [11–13], nickelates [14, 15], organics [16, 17], and magic-angle twisted bilayer graphene [18]. Understanding the interplay between SC and SDW, however, has remained challenging due to the limited tunability of existing materials platforms.

In this connection, quasi-one-dimensional (quasi-1D) models have been extensively studied as they naturally exhibit non-Fermi liquid physics. Various theoretical proposals have explored the emergence of SC and SDW phases and the conditions under which they coexist or compete [19–22]. Higher-dimensional correlated systems can be obtained by coupling multiple 1D wires or chains [23–26] to offer greater control through variation of intra- and inter-wire interactions. Organic superconductors [16, 17] present a promising example of coupled-wire systems [27] for coexisting SC and SDW phases.

Recent studies of double helical edge states (DHESs) in double quantum spin Hall insulators (DQSHIs) indicate that these states can host a higher-order topological phase [28–31], and may also stabilize new phases supporting Majorana Kramers pairs [32]. Originating from the non-trivial band topologies found in DQSHIs [33–37], the associated DHESs have been identified in

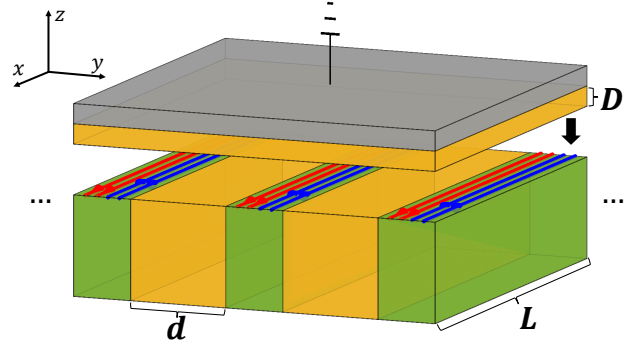


FIG. 1. A schematic sectional view of the double quantum spin Hall superlattice. The grey, green, and yellow regions indicate the grounded metallic gate, the DQSHIs, and the embedding dielectric materials, respectively. Red and blue arrows indicate the up- and down-spin states forming the DHESs. Black arrow indicates the direction of coverage, highlighting the interface between the two parts.

numerous materials for potential realization [30, 38–49]. Unlike the single helical edge states, interactions transform DHESs into a two-channel Luttinger liquid (LL) [32], which resembles the Luther-Emery liquid characterized by a gapless charge sector and a gapped spin sector [23, 50]. Collective excitations within the DHESs remain helical due to the helical nature of the underlying single-particle excitations. Considering the potential of coupled Luther-Emery liquid arrays for supporting competing two-dimensional (2D) SC and CDW phases [23, 24], it is natural to ask if an array of coupled DHESs could also support such competing phases.

In this study, we analyze weakly coupled DHESs emerging from the surface of a double quantum spin Hall superlattice of length L , created by embedding dielectric materials of thickness d periodically between DQSHIs along the out-of-plane direction. Next, the superlattice

* Contact author: hung.yi@northeastern.edu

† Contact author: ar.bansil@northeastern.edu

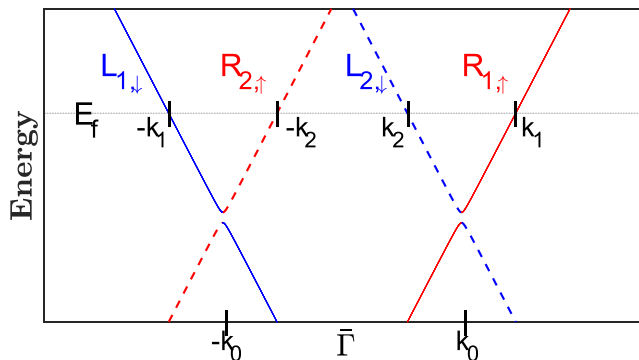


FIG. 2. A schematic of the dispersion of DHESs near the Fermi level, E_f . The right-(left-)moving modes are labeled as $R_{\mu,\uparrow}$ ($L_{\mu,\downarrow}$), where the index $\mu = 1, 2$ denotes the two time-reversal sectors represented by the solid and dashed bands. $k_0 \equiv (k_1 + k_2)/2$ denotes the midpoint of the edge states' momentum.

is coated with a dielectric material of thickness D , and a grounded metallic gate is added on top, see Fig. 1. We show that the inter-edge interaction approximately develops a helical sliding Luttinger liquid (HSSL) order with parameters tunable by the embedded dielectric materials. Importantly, we demonstrate that symmetry-allowed inter-edge tunnelings suggest competing 2D π -SC and π -SDW phases over a certain range of parameters through a renormalization group (RG) analysis to the lowest order. We discuss the potential materials realization of DQSHIs. Our system offers a versatile platform for realizing competing π -SC and π -SDW phases.

II. SETUP

A. The Double Helical Edge States (DHESs)

DHESs host two pairs of helical edge states, which transform independently under time-reversal symmetry [31]. These low-energy states can be represented by the fermionic fields:

$$\psi_\mu(r) = R_{\mu\uparrow}(r)e^{-i(-1)^\mu k_\mu r} + L_{\mu\downarrow}(r)e^{i(-1)^\mu k_\mu r}, \quad (1)$$

where the index $\mu = 1, 2$ indicates the time-reversal sectors (Fig. 2). We suppress the spin index in Eq. (1) from now on for simplicity.

When the forward scatterings are included in the DHESs, the system develops a two-channel LL featuring a gapless charge sector and a gapped pseudospin sector. Specifically, a mass term, arising from e - e interactions or spin-orbit coupling, induces the gap in the pseudospin sector with the following bosonization representation:

$$H_m = \frac{m}{2(\pi a)^2} \int dr \cos[2\sqrt{2}\vartheta_\tau(r)], \quad (2)$$

where the index τ indicates the pseudospin sector; see Appendix A for details of the bosonization convention.

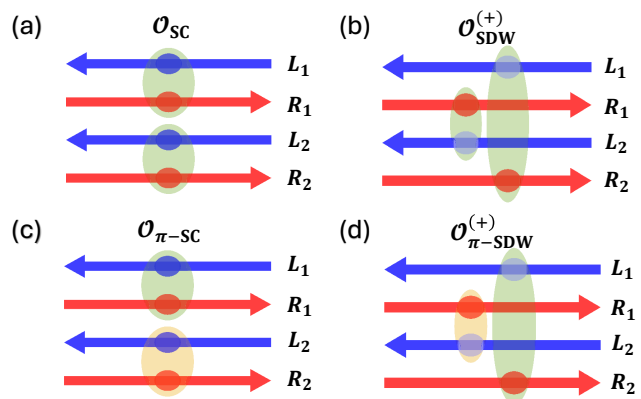


FIG. 3. Schematic diagrams illustrating excitations in (a) SC, (b) SDW, (c) π -SC, and (d) π -SDW phases. Only the excitations corresponding to the $\mathcal{O}_{(\pi)\text{-SDW}}^{(+)}$ for SDW phases are shown without loss of generality. Filled (empty) spheres represent electrons (holes). Green and yellow clouds around the two spheres indicate the formation of electron-electron pairs for (π)-SC or electron-hole pairs for (π)-SDW phases. There is a π -phase difference between the pairs with green and yellow clouds corresponding to Eqs. (3) and (4).

In contrast to the single helical edge states [51], such a mass term does not require a broken time-reversal symmetry in DHESs and originates from the forward scattering between different time-reversal sectors tied to the long-range component of the interacting potential [32] or the second-order effect from the spin-orbit coupling; see Appendix B for details.

In the presence of the mass term, $2\sqrt{2}\vartheta_\tau(r) \bmod 2\pi$ becomes pinned at $0, \pi$ on the mesoscopic scale and gives rise to phases like SC and SDW for $m < 0$, and their π -junction counterparts (π -SC and π -SDW) for $m > 0$; the nomenclature denotes a π -phase difference between time-reversal sectors. The operators characterizing the corresponding instabilities are:

$$\mathcal{O}_{(\pi)\text{-SC}}(r) \propto R_1^\dagger(r)L_1^\dagger(r) - L_1^\dagger(r)R_1^\dagger(r) \pm (1 \leftrightarrow 2), \quad (3)$$

$$\mathcal{O}_{(\pi)\text{-SDW}}^{(+)}(r) \propto R_2^\dagger(r)L_1(r) \pm (1 \leftrightarrow 2), \quad (4)$$

$$\mathcal{O}_{(\pi)\text{-SDW}}^{(-)}(r) \propto L_1^\dagger(r)R_2(r) \pm (1 \leftrightarrow 2), \quad (5)$$

where $\mathcal{O}_{(\pi)\text{-SDW}}^{(\pm)} \equiv \mathcal{O}_{(\pi)\text{-SDW}}^{(x)} \pm i\mathcal{O}_{(\pi)\text{-SDW}}^{(y)}$ characterize the instabilities of in-plane components of (π)-SDW. A schematic diagram of the related excitations is shown in Fig. 3. Note that the four schematics in Fig. 3, along with their Hermitian conjugates, represent the relevant scattering processes between the left- and right-moving modes in the DHESs within a single edge channel. Other processes do not correspond to RG-relevant instabilities with divergent susceptibilities [32].

B. Inter-edge Tunnelings

Upon coupling DHESs on different edges in an array (Fig. 1), the single-particle inter-edge tunneling becomes irrelevant due to the gapped pseudospin sector [23]. The remaining relevant tunnelings are essentially two-body inter-edge tunnelings in the SC and SDW channels. Due to time-reversal symmetry, the allowed two-body inter-edge tunnelings are of the form:

$$H_{(\pi^-)\text{SC}}^{(\text{inter})} = - \sum_{i \neq j} J_{\text{SC},|i-j|} \times \int dr \mathcal{O}_{(\pi^-)\text{SC},i}^\dagger(r) \mathcal{O}_{(\pi^-)\text{SC},j}(r), \quad (6)$$

$$H_{(\pi^-)\text{SDW}}^{(\text{inter})} = - \sum_{i \neq j} J_{\text{SDW},|i-j|} \times \int dr \mathcal{O}_{(\pi^-)\text{SDW},i}^{(+)}(r) \mathcal{O}_{(\pi^-)\text{SDW},j}^{(-)}(r). \quad (7)$$

Here, $J_{\text{SC},|i-j|}$ and $J_{\text{SDW},|i-j|}$ indicate the strength of the inter-edge tunneling for the $(\pi^-)\text{SC}$ and $(\pi^-)\text{SDW}$ channels between i th and j th edges, and $\mathcal{O}_{(\pi^-)\text{SC},i}$ and $\mathcal{O}_{(\pi^-)\text{SDW},i}^{(\pm)}$ denote operators characterizing instability of $(\pi^-)\text{SC}$ and the in-plane components of $(\pi^-)\text{SDW}$ on the i th edge. The $(\pi^-)\text{SC}$ and $(\pi^-)\text{SDW}$ channels represent pair tunneling with particle-particle and particle-hole pairs in the charge sector, respectively [23, 53]. Due to the helical nature of the charge sector, the particle-hole pairs resemble the electronic spin [32]. Thus, the corresponding inter-edge tunneling develops a 2D $(\pi^-)\text{SDW}$ phase when it becomes relevant.

The inter-edge tunnelings have the following bosonization representations:

$$H_{(\pi^-)\text{SC}}^{(\text{inter})} \sim - \sum_{i \neq j} \frac{J_{\text{SC},|i-j|}}{(\pi a)^2} \int dr e^{i\sqrt{2}\vartheta_{c,i}(r)} e^{-i\sqrt{2}\vartheta_{c,j}(r)} \times f_{(\pi)}[\sqrt{2}\vartheta_{\tau,i}(r)] f_{(\pi)}[\sqrt{2}\vartheta_{\tau,j}(r)], \quad (8)$$

$$H_{(\pi^-)\text{SDW}}^{(\text{inter})} \sim - \sum_{i \neq j} \frac{J_{\text{SDW},|i-j|}}{(\pi a)^2} \int dr e^{i\sqrt{2}\varphi_{c,i}(r)} e^{-i\sqrt{2}\varphi_{c,j}(r)} \times f_{(\pi)}[\sqrt{2}\vartheta_{\tau,i}(r)] f_{(\pi)}[\sqrt{2}\vartheta_{\tau,j}(r)], \quad (9)$$

where the index c indicates the charge sector and $f(x) = \cos(x)$ with $f_{\pi}(x) = \sin(x)$. Note that the gap in the pseudospin sector on each edge is developed by Eq. (2). Therefore, for $m > 0$, $\sqrt{2}\vartheta_{\tau}(r)$ is pinned at $(n + 1/2)\pi$, $H_{\pi^- \text{SC}}^{(\text{inter})}$ and $H_{\pi^- \text{SDW}}^{(\text{inter})}$ are favored. Similarly, $H_{\text{SC}}^{(\text{inter})}$ and $H_{\text{SDW}}^{(\text{inter})}$ are favored for $m < 0$. Deep in the phase where m is relevant, we can absorb the fields in the pseudospin sector by their mesoscopic expectation values [23] and

further simplify the inter-edge tunnelings into:

$$H_{(\pi^-)\text{SC}}^{(\text{inter})} = - \sum_{i \neq j} \frac{J_{\text{SC},|i-j|}}{(\pi a)^2} \int dr e^{i\sqrt{2}[\vartheta_{c,i}(r) - \vartheta_{c,j}(r)]}, \quad (10)$$

$$H_{(\pi^-)\text{SDW}}^{(\text{inter})} = - \sum_{i \neq j} \frac{J_{\text{SDW},|i-j|}}{(\pi a)^2} \int dr e^{i\sqrt{2}[\varphi_{c,i}(r) - \varphi_{c,j}(r)]}. \quad (11)$$

C. Helical Sliding Luttinger Liquid

Besides the inter-edge tunneling, different edges are also coupled through inter-edge forward scattering. Note that screened Coulomb interactions modify only the charge-sector interaction parameters. Upon a Fourier transform in the transverse direction, we obtain a helical sliding Luttinger liquid (HSSL) described by,

$$H_{\text{HSSL}} = \int dr \int_{-\pi}^{\pi} \frac{dk_{\perp}}{2\pi} \frac{\hbar u}{2\pi} [K_{k_{\perp}}^{-1}(\partial_r \varphi_{k_{\perp}}(r))^2 + K_{k_{\perp}}(\partial_r \vartheta_{k_{\perp}}(r))^2], \quad (12)$$

which can be viewed as a helical version of the sliding Luttinger liquid [53] or a smectic metal [54]. Here $K_{k_{\perp}}$ denotes the HSSL parameter for the $\varphi_{k_{\perp}}(r)$ and $\vartheta_{k_{\perp}}(r)$ fields with dimensionless transverse momentum k_{\perp} , and u denotes the renormalized velocity.

Considering a heterostructure with sufficiently weak inter-edge couplings and a sufficiently large inter-edge distance, we expand the HSSL parameter $K_{k_{\perp}}$ to the first harmonic of the transverse momentum; see Appendix C for details:

$$K_{k_{\perp}} \cong K_0 [1 + K_1 \sin(|k_{\perp}|)], \quad (13)$$

where

$$K_0 = \sqrt{\frac{1}{1 + \frac{2e^2 D}{\hbar v \pi \epsilon d}}}, \quad (14)$$

$$K_1 = \frac{2e^2 D^2}{\hbar v \pi \epsilon d^2}. \quad (15)$$

Here, v is the Fermi velocity of the helical edge states, ϵ refers to the dielectric constant of the double quantum spin Hall superlattice, d is the inter-edge distance, and D is the distance between the edge states and the metallic gate. A large inter-edge distance ($d \gg D$) indicates a well-screened system. We assume similar dielectric constants for the DQSHI and the dielectric material in Eqs. (14) and (15) for simplicity.

Given a sufficiently large inter-edge distance, only the nearest-neighbor inter-edge tunnelings, $J_{\text{SC},1}$ and $J_{\text{SDW},1}$ are relevant, although it is straightforward to include terms beyond the nearest-neighboring DQSHI edges. We show below how inter-edge tunnelings lead to competing 2D $(\pi^-)\text{SC}$ and $(\pi^-)\text{SDW}$ phases.

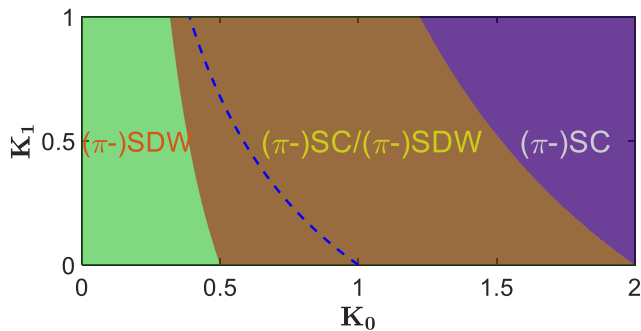


FIG. 4. Generic phase diagram as a function of the interaction parameters: green, brown, and purple colors indicate the regions of (π) -SDW, competing (π) -SDW and (π) -SC, and (π) -SC phases, respectively. Blue dashed line shows where the scaling dimensions of operators for (π) -SDW and (π) -SC phases are the same.

III. PHASE DIAGRAM

We derive the RG flow equations for the two-body inter-edge tunneling from co-tunneling processes up to the leading order [23, 55]:

$$\frac{d\tilde{J}_{\text{SC},1}}{dl} = \left[2 - \frac{1}{K_0} \frac{2 \cos^{-1}(K_1)}{\pi \sqrt{1 - K_1^2}} \right] \tilde{J}_{\text{SC},1}, \quad (16)$$

$$\frac{d\tilde{J}_{\text{SDW},1}}{dl} = \left[2 - K_0 \left(1 + \frac{2K_1}{\pi} \right) \right] \tilde{J}_{\text{SDW},1}, \quad (17)$$

where $l \equiv \ln[a(l)/a(0)]$, a is the cutoff of the low-energy theory, and $\tilde{J}_{[\dots],N} \equiv J_{[\dots],N}/\hbar v \pi^2$ are dimensionless two-body inter-edge tunnelings; see Appendix D for details. According to Eqs. (16) and (17), the $\tilde{J}_{(\pi)\text{SC},1}$ is RG relevant for $K_0 > \cos^{-1}(K_1)/(\pi \sqrt{1 - K_1^2})$. The $\tilde{J}_{(\pi)\text{SDW},1}$ is RG relevant for $K_0 < 2/(1 + 2K_1/\pi)$. This implies a regime with $\cos^{-1}(K_1)/(\pi \sqrt{1 - K_1^2}) < K_0 < 2/(1 + 2K_1/\pi)$, in which both the (π) -SC and (π) -SDW phases are RG relevant and compete. Figure 4 summarizes the resulting phase diagram. The determination of whether the competing SC and SDW phases or the π -SC and π -SDW phases are at play depends on the sign of the mass in Eq. (2). We emphasize that although higher-order RG analysis can in principle provide more precise phase boundaries, it is not expected to introduce new phases or new regimes of competing orders.

Beyond the phase diagram, a comprehensive RG analysis also uncovers the source of two-body inter-edge tunnelings, which can arise from the second-order contributions of single-particle inter-edge tunneling t_\perp (co-tunneling). This is clearly reflected in the schematic RG flow equations $d\tilde{J}/dl = (2 - \eta)\tilde{J} + \mathcal{O}(t_\perp^2)$, see Appendix D for details. In this way, even though $\tilde{J}_{(\pi)\text{SC},1}(l=0)$ and $\tilde{J}_{(\pi)\text{SDW},1}(l=0)$ are initially zero, non-zero values of $\tilde{J}_{(\pi)\text{SC},1}$ and $\tilde{J}_{(\pi)\text{SDW},1}$ can emerge through the RG flow due to $t_\perp(l=0) \neq 0$, although t_\perp is considered RG irrelevant due to the gapped pseudospin sector [23].

IV. POTENTIAL PLATFORMS

We now turn to discuss how we could realize heterostructures that host HSSL and competing SC and SDW orders. We first consider the DHESs whose existence has been experimentally and theoretically demonstrated in various topological materials such as spin and mirror Chern insulators with the associated spin and mirror Chern numbers of ± 2 . Experimentally realized platforms include bilayer β -Bi₄Br₄ [38, 39], twisted bilayer MoTe₂ [43, 56] and WSe₂ [44], thin films of the SnTe family [46–49], and coupled HgTe quantum wells [57–62]. Additional candidate materials proposed by first-principles calculations include α -antimonene [40], RuBr₃ [30, 41], the oxide compound (MO₂)₂(ZrO₂)₄ with M = Pt, W [42], and Na₂CdSn [45]. Notably, the spin-valley locking in transition-metal dichalcogenides (TMDs) such as MoTe₂ and WSe₂ ensures spin- $U(1)$ symmetry in their twisted bilayers, facilitating the realization of the DHESs.

Note that the predominant screened Coulomb interaction would lead to $m > 0$ in the pseudospin sector [32] and thus favor the π -SC and π -SDW phases, as discussed in Sec. II A. But, for a given DQSHI, the HSSL parameters given in Eqs. (14) and (15) could be straightforwardly adjusted through the inter-edge separation d and the screening distance to the metallic gate D such that $1/\pi < K_0 < 1$ and $0 < K_1 \ll 1$, driving the system into the regime of phase competition. This expectation can be further substantiated by estimating the interaction strength based on material-specific parameters for MoTe₂ and WSe₂ [56, 63, 64]; the corresponding phase diagram is shown in Fig. 5. Assuming $D/d \ll 1$ in Eqs.(14) and (15), and using $\hbar v \approx \mathcal{O}(10^{-11})$ eV · m [56] and $\epsilon \approx 10\epsilon_0$ [63, 64] for twisted bilayer MoTe₂ and WSe₂, our analysis reveals the presence of competing π -SC and π -SDW phases over a wide parameter range, see Fig. 5. Based on the RG flow in Eqs. (16) and (17), we can determine the minimal edge length L^* necessary to reach the strong-coupling regime, where the dimensionless inter-edge tunnelings attain $\mathcal{O}(1)$:

$$L^* = \min_{\alpha \in \{\text{SC}, \text{SDW}\}} \left(a(0) [\tilde{J}_\alpha(l \rightarrow 0)]^{-\frac{1}{2-\eta_\alpha}} \right), \quad (18)$$

where $\eta_{\text{SC}} = 2 \cos^{-1}(K_1)/\pi K_0 \sqrt{1 - K_1^2}$ and $\eta_{\text{SDW}} = K_0(1 + 2K_1/\pi)$. To estimate L^* in twisted-bilayer-TMD-based double quantum spin Hall materials, we use $a(0) \approx 4$ nm [56] and $\tilde{J}_\alpha(l \rightarrow 0) \approx 10^{-4}$. This choice follows from estimating $\tilde{J}_\alpha(l \rightarrow 0)$ as $(t_\perp(l=0)/\hbar v)^2$, with $t_\perp \approx 10^{-2} \hbar v/a$ chosen to align with the energy scale hierarchy in Eq. (19), see Appendix D and the following section for details. The associated characteristic temperature T^* can also be determined by $T^* = \hbar v/k_B L^*$, marking the temperature scale below which the system enters the strong-coupling regime. Figures 5 and 6 summarize the preceding estimates and demonstrate that a rich phase diagram can arise from competing π -SC and π -SDW phases below $\mathcal{O}(100)$ mK in devices larger than

$O(\mu\text{m})$.

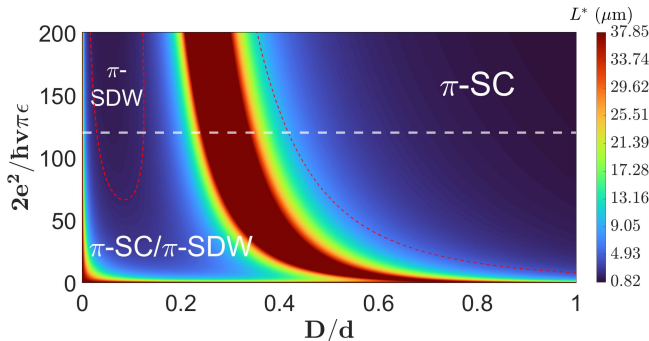


FIG. 5. Phase diagram and minimal edge length L^* in Eq. (18) estimated with $a(0) \approx 4$ nm and $\bar{J}_\alpha(l \rightarrow 0) \approx 10^{-4}$ as functions of system parameters defined in Eqs. (14) and (15). Red dashed lines mark phase boundaries, and the colormap indicates the L^* values below which the system remains in the HSSL phase. The white dashed line marks an estimated (order of magnitude) parameter regime relevant for twisted-bilayer-TMD based double quantum spin Hall superlattices using MoTe_2 and WSe_2 .

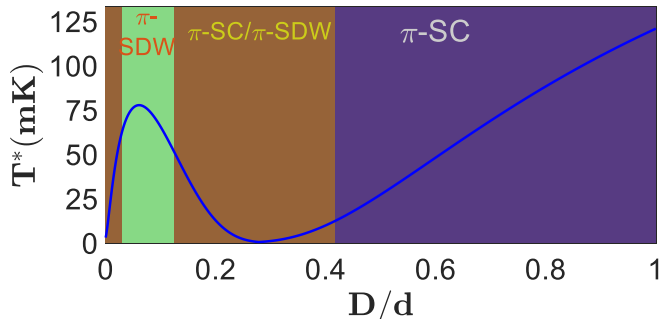


FIG. 6. Characteristic temperature T^* for various phases in the twisted-bilayer MoTe_2 - or WSe_2 -based double quantum spin Hall superlattices, estimated from the parameter set corresponding to the white dashed line in Fig. 5. Colored regions correspond to the phases indicated in Fig. 4.

Regarding the energy hierarchy in our analysis, note that we have explored weak inter-edge couplings, focusing solely on the nearest-neighbor tunnelings, and expanding the HSSL parameter to the first harmonic of the transverse momentum. Weak inter-edge couplings ensure that the gap in the pseudospin sector develops first to avoid a dimensional crossover, yielding the energy scale hierarchy:

$$\frac{\hbar v}{a} \gg U_{2k_0} \gg t_\perp. \quad (19)$$

Here, v and a are the Fermi velocity and cutoff of the low-energy theory, respectively. U_q is the Fourier component of the intra-edge density-density interaction with momentum q . The hierarchy in Eq. (19) implies that the

RG-relevant mass term (set by U_{2k_0}) gaps out the pseudospin sector at a much higher energy scale than the inter-edge tunneling t_\perp . This justifies treating the ϑ_τ field as pinned and focusing only on the RG flow of the two-body inter-edge tunneling in the effective low-energy theory (c.f. Eqs. (16) and (17)), where single-particle inter-edge tunneling remains RG irrelevant. Practically, these weak inter-edge couplings could be realized by maintaining a large distance between the edges during the fabrication of the superlattice structure.

V. SUMMARY

DQSHIs host DHESs, which yield unique π -SC and π -SDW phases driven by the long-range intra-edge forward scattering. These unconventional electronic orders are distinct from the conventional SC and SDW phases that arise from Fermi surface instabilities of Luttinger liquid physics. Inspired by the intricate phase competition in coupled quantum wire systems, we propose using the side surface of a double quantum spin Hall superlattice to realize an array of coupled DHESs by stacking double quantum spin Hall layers alternating with dielectrics. Our analysis demonstrates that such an array can provide a tunable platform for exploring competing 2D π -SC and π -SDW phases through the RG-relevant particle-particle and particle-hole inter-edge tunnelings. Further inter-edge tunnelings and higher-harmonic components of the HSSL parameter could be introduced by adjusting the inter-edge distance and dielectric constant through device fabrication to yield a new playground for investigating unconventional electronic orders more generally.

ACKNOWLEDGEMENT

The work at Northeastern University was supported by the Air Force Office of Scientific Research under award number FA9550-20-1-0322 and benefited from the resources of Northeastern University's Advanced Scientific Computation Center, the Discovery Cluster, the Quantum Materials and Sensing Institute, and the Massachusetts Technology Collaborative award MTC-22032. C.-H.H. acknowledges the support from the National Science and Technology Council (NSTC), Taiwan, through Grant No. NSTC-112-2112-M-001-025-MY3 and Academia Sinica (AS), Taiwan, through Grant No. AS-iMATE-114-12.

DATA AVAILABILITY

The results shown in Figs. 4, 5, and 6 can be reproduced by the codes on GitHub [65], where the data that support the findings of this article are openly available.

Appendix A: Bosonization convention

The DHESs host two left- and right-moving modes carrying different spin, forming two pairs of time-reversal partners in the time-reversal sector with the following bosonization expression [66]:

$$\begin{aligned} R_{\mu,i,\uparrow}(r) &= \frac{\kappa_R}{\sqrt{2\pi a}} e^{i[\vartheta_{\mu,i}(r) - \varphi_{\mu,i}(r)]}, \\ L_{\mu,i,\downarrow}(r) &= \frac{\kappa_L}{\sqrt{2\pi a}} e^{i[\vartheta_{\mu,i}(r) + \varphi_{\mu,i}(r)]}, \end{aligned} \quad (\text{A1})$$

where i is the edge index and $\mu = 1, 2$ indicates the time-reversal sector and a is the cutoff. The bosonic fields satisfy the commutation relation $[\varphi_{\mu,i}(r), \vartheta_{\nu,j}(r')] = -i\frac{\pi}{2}\text{sgn}(r-r')\delta_{ij}\delta_{\mu\nu}$ for $\mu, \nu = 1, 2$ [23], and can be further expressed in terms of charge (c) and pseudospin (τ) sectors through:

$$\begin{pmatrix} \varphi_{c,i}(r) \\ \varphi_{\tau,i}(r) \end{pmatrix} \equiv \frac{1}{\sqrt{2}} \begin{pmatrix} 1 & 1 \\ 1 & -1 \end{pmatrix} \begin{pmatrix} \varphi_{1,i}(r) \\ \varphi_{2,i}(r) \end{pmatrix} \quad (\text{A2})$$

$$\begin{pmatrix} \vartheta_{c,i}(r) \\ \vartheta_{\tau,i}(r) \end{pmatrix} \equiv \frac{1}{\sqrt{2}} \begin{pmatrix} 1 & 1 \\ 1 & -1 \end{pmatrix} \begin{pmatrix} \vartheta_{1,i}(r) \\ \vartheta_{2,i}(r) \end{pmatrix}, \quad (\text{A3})$$

satisfying $[\vartheta_{\mu,j}(r'), \varphi_{\nu,i}(r)] = i\frac{\pi}{2}\text{sgn}(r-r')\delta_{ij}\delta_{\mu\nu}$ for $\mu, \nu = c, \tau$ [32].

Appendix B: Second-order effect of the spin-orbit coupling (SOC)

In DHESs of DQSHIs, the edge Dirac points are solely protected by the spin-U(1) symmetry, so that any spin-U(1) symmetry-breaking perturbation, such as SOC, gaps the edge Dirac cones, see Fig. 2. Such a SOC term is described by the Hamiltonian:

$$H_{\text{SOC}} = \lambda \int dr \left[e^{i\theta} R_1^\dagger(r) L_2(r) + e^{-i(\theta+\pi)} R_2^\dagger(r) L_1(r) + \text{H.c.} \right], \quad (\text{B1})$$

where λ and θ describe the strength and phase of the SOC, respectively [31]. This perturbation is RG relevant when the Fermi level is located at the edge Dirac points. However, if the Fermi level is above the edge Dirac point, which is the case considered here, it turns into a rapidly oscillating term and becomes irrelevant. Still, its second-order effect is relevant and has the following form:

$$-\lambda^2 \int dr R_1^\dagger(r) L_2(r) L_1^\dagger(r) R_2(r) + \text{H.c.}, \quad (\text{B2})$$

which is proportional to the fermionic expression of the mass term in Eq. (2) of the main text. Equation (B2) contributes to this mass term via the second-order RG flow equation through

$$\frac{d\tilde{m}}{dl} = 2(1 - K_\tau^{-1})\tilde{m} + \mathcal{O}(\lambda^2), \quad (\text{B3})$$

where $\tilde{m} \equiv m/\hbar v$, v is the fermi velocity, and K_τ is the LL parameter of the pseudospin sector [32].

Appendix C: Helical sliding Luttinger liquid (HSLL)

Here we derive the HSLL fixed point Hamiltonian and compute the parameters renormalized by the forward scatterings from the screened Coulomb interaction in the double quantum spin Hall superlattice in Fig. 1 of the main text.

1. Screened Coulomb interaction in double quantum spin Hall superlattice

To derive the screened Coulomb potential $V(\mathbf{x})$ in the double quantum spin Hall superlattice, we begin with the Poisson equation:

$$-\nabla^2 V(\mathbf{x}) = \frac{1}{\epsilon} \rho(\mathbf{x}). \quad (\text{C1})$$

For simplicity, we will assume similar values of the dielectric constant (ϵ) for both the DQSHI and the dielectric material. Since the helical edge states are confined to a 2D plane, we place the charge density on $z = 0$ plane, away from a metallic gate positioned at $z = D$. We thus rewrite Eq. (C1) as:

$$(q_x^2 + q_y^2 - \partial_z^2) V(\mathbf{q}, z) = \frac{1}{\epsilon} \rho_{2D}(\mathbf{q}) \delta(z). \quad (\text{C2})$$

Here, we have Fourier transformed the density from $\rho(\mathbf{x})$ to $\rho_{2D}(\mathbf{q})\delta(z)$ due to the charge localization on the $z = 0$ plane. By assuming the ansatz for the potential to be $V(\mathbf{q}, z) = V_{2D}(\mathbf{q})V_\perp(z)$, we obtain:

$$V_\perp(z) = A^{>(<)} e^{qz} + B^{>(<)} e^{-qz}, \text{ for } z > 0 (z < 0), \quad (\text{C3})$$

where $q \equiv |\mathbf{q}|$. The metallic gate at $z = D$ imposes the following Dirichlet boundary conditions:

$$V_\perp(z = D) = V_\perp(z \rightarrow \infty) = 0 \quad (\text{C4})$$

leading to $B^{<} = 0$ and $B^{>} = -A^{>} e^{2qD}$. Since the potential is continuous across the $z = 0$ plane, we also have $A^{<} = A^{>} (1 - e^{2qD})$. To derive $A^{>}$, we apply Gauss's law on a flat surface enclosing $z = 0$ plane, which yields $-\partial_z V_\perp|_{0^-}^{0^+} = \frac{1}{\epsilon} \frac{\rho_{2D}(\mathbf{q})}{V_{2D}(\mathbf{q})}$ and, hence,

$$A^{>} = \frac{-e^{-2qD} \rho_{2D}(\mathbf{q})}{2q\epsilon V_{2D}(\mathbf{q})}. \quad (\text{C5})$$

Using the above results, the potential on the $z = 0$ plane is

$$V(\mathbf{x}, z = 0) = \int \frac{d^2 q}{(2\pi)^2} e^{i\mathbf{q}\cdot\mathbf{x}} \rho_{2D}(\mathbf{q}) \frac{(1 - e^{-2qD})}{2\epsilon q}. \quad (\text{C6})$$

2. HSLL Hamiltonian

In DHESs, intra-edge potentials with non-zero momentum can renormalize the kinetic terms [32]. However, since the zero-momentum component dominates the

screened Coulomb potential, we neglect the contribution from the finite-longitudinal-momentum components to the renormalization of the kinetic terms for simplicity, as they do not significantly change the physics. For the double quantum spin Hall superlattice, the charge density can be expressed as:

$$\rho_{2D}(\mathbf{x}) = e \sum_{m=1}^{N_{\perp}} \rho_m(x) \delta(y - md), \quad (\text{C7})$$

where N_{\perp} is the number of edges in the superlattice, and d is the inter-edge distance. Then, the electron-electron interaction is:

$$\begin{aligned} H_{ee} &= \frac{1}{2} \int d^2x \rho_{2D}(x) V_{2D}(\mathbf{x}) \\ &= \frac{e^2}{4\epsilon} \int d^2x \sum_{m=1}^{N_{\perp}} \rho_m(x) \delta(y - md) \\ &\quad \times \int \frac{d^2q}{(2\pi)^2} e^{i\mathbf{q}\cdot\mathbf{x}} \frac{(1 - e^{-2qD})}{q} \\ &\quad \times \int d^2x' \sum_{m'=1}^{N_{\perp}} \rho_{m'}(x') \delta(y' - md) e^{-i\mathbf{q}\cdot\mathbf{x}'}. \end{aligned} \quad (\text{C8})$$

Since we focus on contributions from zero-longitudinal-momentum $q_x \rightarrow 0$ for the HSSL parameters and the renormalized velocities, the Hamiltonian in Eq. (C8) is approximately:

$$\begin{aligned} H_{ee} &\cong \frac{e^2}{4\epsilon d} \int dx' \sum_{m,m'=1}^{N_{\perp}} \rho_m(x') \rho_{m'}(x') \\ &\quad \times \frac{1}{2\pi N_{\perp}} \sum_{q_y} e^{iq_y(m-m')d} \frac{(1 - e^{-2|q_y|D})}{|q_y|}. \end{aligned} \quad (\text{C9})$$

Here, we have used the discrete sum for the Fourier transform in the perpendicular direction. By defining the dimensionless transverse momentum $k_{\perp} \equiv q_y d$ and considering the limit of $N_{\perp} \rightarrow \infty$, we can further bosonize Eq. (C9) into:

$$H_{ee} = \frac{e^2}{2\pi^2 \epsilon} \int \frac{dk_{\perp}}{2\pi} \int dr |\partial_r \varphi_{k_{\perp}}(r)|^2 \frac{(1 - e^{-2|k_{\perp}|D/d})}{|k_{\perp}|}. \quad (\text{C10})$$

Together with the kinetic energy terms, we get

$$\begin{aligned} H &= \int \frac{dk_{\perp}}{2\pi} \int dr \left[\frac{\hbar v}{2\pi} + \frac{e^2(1 - e^{-2|k_{\perp}|D/d})}{2\pi^2 \epsilon |k_{\perp}|} \right] |\partial_r \varphi_{k_{\perp}}|^2 \\ &\quad + \frac{\hbar v}{2\pi} |\partial_r \vartheta_{k_{\perp}}|^2, \end{aligned} \quad (\text{C11})$$

which leads to the HSSL parameter and the renormalized velocity:

$$K_{k_{\perp}} = \sqrt{\frac{1}{1 + \frac{e^2(1 - e^{-2|k_{\perp}|D/d})}{\hbar v \pi \epsilon |k_{\perp}|}}}, \quad (\text{C12})$$

$$u_{k_{\perp}} = v \sqrt{1 + \frac{e^2(1 - e^{-2|k_{\perp}|D/d})}{\hbar v \pi \epsilon |k_{\perp}|}}. \quad (\text{C13})$$

We further consider a large inter-edge distance ($d \gg D$) and the long-wavelength limit $|k_{\perp}| \ll 1$, leading to the HSSL parameter and the renormalized velocity corresponding to the Hamiltonian in Eq. (C11) to be:

$$\begin{aligned} K_{k_{\perp}} &\cong \sqrt{\frac{1}{1 + \frac{2e^2 D}{\hbar v \pi \epsilon d} - \frac{4e^2 D^2 |k_{\perp}|}{\hbar v \pi \epsilon d^2}}} \\ &\cong \sqrt{\frac{1}{1 + \frac{2e^2 D}{\hbar v \pi \epsilon d}} \left(1 + \frac{2e^2 D^2 |k_{\perp}|}{\hbar v \pi \epsilon d^2 (1 + \frac{2e^2 D}{\hbar v \pi \epsilon d})} \right)} \\ &\cong \sqrt{\frac{1}{1 + \frac{2e^2 D}{\hbar v \pi \epsilon d}} \left(1 + \frac{2e^2 D^2}{\hbar v \pi \epsilon d^2} \sin(|k_{\perp}|) \right)}, \end{aligned} \quad (\text{C14})$$

$$u_{k_{\perp}} \cong v \sqrt{1 + \frac{2e^2 D}{\hbar v \pi \epsilon d}} \equiv u. \quad (\text{C15})$$

recovering Eqs. (14) and (15) of the main text.

Appendix D: Renormalization-group (RG) flow equations

To derive the RG flow equations for the phase diagram, we first Fourier transform the two-body inter-edge tunnelings in Eqs. (10) and (11) in the transverse direction:

$$\begin{aligned} H_{\text{SC}}^{(\text{inter})} &= - \sum_{i \neq j} \frac{J_{\text{SC},|i-j|}}{(\pi a)^2} \\ &\quad \times \int dr e^{-i2\sqrt{2} \int \frac{dk_{\perp}}{2\pi} [\vartheta_{k_{\perp}}(r) \sin(\frac{i-j}{2} k_{\perp}) \sin(\frac{i+j}{2} k_{\perp})]}, \end{aligned} \quad (\text{D1})$$

$$\begin{aligned} H_{\text{SDW}}^{(\text{inter})} &= - \sum_{i \neq j} \frac{J_{\text{SDW},|i-j|}}{(\pi a)^2} \\ &\quad \times \int dr e^{-i2\sqrt{2} \int \frac{dk_{\perp}}{2\pi} [\varphi_{k_{\perp}}(r) \sin(\frac{i-j}{2} k_{\perp}) \sin(\frac{i+j}{2} k_{\perp})]}, \end{aligned} \quad (\text{D2})$$

where we have expanded the fields by

$$\vartheta_{c,i}(r) = \int \frac{dk_{\perp}}{2\pi} \vartheta_{k_{\perp}}(r) \cos(ik_{\perp}), \quad (\text{D3})$$

$$\varphi_{c,i}(r) = \int \frac{dk_{\perp}}{2\pi} \varphi_{k_{\perp}}(r) \cos(ik_{\perp}). \quad (\text{D4})$$

Then, together with Eq. (12), the perturbative RG flow equations to the leading order contribution can be derived through a standard procedure [55]:

$$\frac{d\tilde{J}_{\text{SC},N}}{dl} = (2 - \eta_{\text{SC},N}) \tilde{J}_{\text{SC},N}, \quad (\text{D5})$$

$$\frac{d\tilde{J}_{\text{SDW},N}}{dl} = (2 - \eta_{\text{SDW},N}) \tilde{J}_{\text{SDW},N}, \quad (\text{D6})$$

where $\tilde{J}_{\dots,N} \equiv J_{\dots,N}/\hbar u \pi^2$ are the dimensionless two-body inter-edge tunnelings and $N = |i - j|$ indicates the N th nearest neighbors and:

$$\begin{aligned}
\eta_{\text{SC},N} &= 2 \sum_I \frac{1}{2} \int \frac{dk_{\perp}}{2\pi} \int \frac{dk'_{\perp}}{2\pi} \ln \left[\frac{\langle \vartheta_{k_{\perp}}(r) \vartheta_{k'_{\perp}}(r) \rangle_0 L}{a} \right] 8 \sin\left(\frac{I}{2} k_{\perp}\right) \sin\left(\frac{I}{2} k'_{\perp}\right) \sin\left(\frac{N}{2} k_{\perp}\right) \sin\left(\frac{N}{2} k'_{\perp}\right) \\
&= 2 \int \frac{dk_{\perp}}{2\pi} \int \frac{dk'_{\perp}}{2\pi} \ln \left[\frac{\langle \vartheta_{k_{\perp}}(r) \vartheta_{k'_{\perp}}(r) \rangle_0 L}{a} \right] 4\pi \left(\delta\left(\frac{k_{\perp}}{2} - \frac{k'_{\perp}}{2} + 2\pi m\right) - \delta\left(\frac{k_{\perp}}{2} + \frac{k'_{\perp}}{2} + 2\pi m\right) \right) \sin\left(\frac{N}{2} k_{\perp}\right) \sin\left(\frac{N}{2} k'_{\perp}\right) \\
&= 2 \int \frac{dk_{\perp}}{2\pi} \frac{1}{K_{k_{\perp}}} \sin^2\left(\frac{N}{2} k_{\perp}\right) \\
&= \int \frac{dk_{\perp}}{2\pi} \frac{1 - \cos(Nk_{\perp})}{K_{k_{\perp}}}, \tag{D7}
\end{aligned}$$

$$\begin{aligned}
\eta_{\text{SDW},N} &= 2 \int \frac{dk_{\perp}}{2\pi} \int \frac{dk'_{\perp}}{2\pi} \ln \left[\frac{\langle \varphi_{k_{\perp}}(r) \varphi_{k'_{\perp}}(r) \rangle_0 L}{a} \right] 4\pi \left(\delta\left(\frac{k_{\perp}}{2} - \frac{k'_{\perp}}{2} + 2\pi m\right) - \delta\left(\frac{k_{\perp}}{2} + \frac{k'_{\perp}}{2} + 2\pi m\right) \right) \sin\left(\frac{N}{2} k_{\perp}\right) \sin\left(\frac{N}{2} k'_{\perp}\right) \\
&= \int \frac{dk_{\perp}}{2\pi} K_{k_{\perp}} [1 - \cos(Nk_{\perp})]. \tag{D8}
\end{aligned}$$

For the nearest neighbors with $K_{k_{\perp}} = K_0[1 + K_1 \sin(|k_{\perp}|)]$, we have

$$\eta_{\text{SC},1} = \frac{1}{K_0} \frac{2 \cos^{-1}(K_1)}{\pi \sqrt{1 - K_1^2}}, \tag{D9}$$

$$\eta_{\text{SDW},1} = K_0 \left(1 + \frac{2K_1}{\pi}\right). \tag{D10}$$

The second-order effect of single-particle inter-edge tunneling t_{\perp} can trigger two-body inter-edge tunnelings. Although single-particle tunneling is irrelevant, its second-order effects can introduce the relevant two-body

inter-edge tunnelings [23]. The symmetry-allowed single-particle inter-edge tunneling has the form:

$$\sum_{i \neq j} \sum_{\mu=1,2} \int dr t_{\perp,|i-j|} [R_{\mu,i}^{\dagger}(r) R_{\mu,j}(r) + L_{\mu,i}^{\dagger}(r) L_{\mu,j}(r)]. \tag{D11}$$

Here, we consider a real inter-edge tunneling $t_{\perp,|i-j|} \in \mathbb{R}$ and ignore the fast-oscillating terms. Then, the second-order perturbation to the partition function includes the expectation value of:

$$-\sum_{i \neq j} \sum_{\mu,\nu=1,2} \int dr \frac{t_{\perp,|i-j|}^2}{2} [R_{\mu,i}^{\dagger}(r) R_{\mu,j}(r) + L_{\mu,i}^{\dagger}(r) L_{\mu,j}(r)] [R_{\nu,i}^{\dagger}(r) R_{\nu,j}(r) + L_{\nu,i}^{\dagger}(r) L_{\nu,j}(r) + (i \leftrightarrow j)], \tag{D12}$$

which considers only the second-order effects that do not introduce hoppings between the three edges. This can

be further decomposed into two terms that contribute to the two-body inter-edge tunnelings:

$$T_1 = -\sum_{i \neq j} \sum_{\mu,\nu=1,2} \int dr \frac{t_{\perp,|i-j|}^2}{2} [R_{\mu,i}^{\dagger}(r) R_{\mu,j}(r) L_{\nu,i}^{\dagger}(r) L_{\nu,j}(r) + L_{\mu,i}^{\dagger}(r) L_{\mu,j}(r) R_{\nu,i}^{\dagger}(r) R_{\nu,j}(r)], \tag{D13}$$

$$T_2 = -\sum_{i \neq j} \sum_{\mu,\nu=1,2} \int dr \frac{t_{\perp,|i-j|}^2}{2} [R_{\mu,i}^{\dagger}(r) R_{\mu,j}(r) L_{\nu,i}^{\dagger}(r) L_{\nu,j}(r) + L_{\mu,i}^{\dagger}(r) L_{\mu,j}(r) R_{\nu,i}^{\dagger}(r) R_{\nu,j}(r)]. \tag{D14}$$

The full two-body inter-edge tunneling is $T = T_1 + T_2$,

which can be decomposed into two parts upon bosonization:

$$\begin{aligned}
T_{\text{SC}} &= - \sum_{i \neq j} \sum_{\mu=1,2} \int dr t_{\perp,|i-j|}^2 [e^{-i2\vartheta_{\mu,i}} e^{i2\vartheta_{\mu,j}} + e^{-i2\varphi_{\mu,i}} e^{i2\varphi_{\mu,j}}] \\
&\propto - \sum_{i \neq j} \int dr t_{\perp,|i-j|}^2 \left\{ e^{-i\sqrt{2}(\vartheta_{c,i}-\vartheta_{c,j})} \cos[\sqrt{2}(\vartheta_{\tau,i}-\vartheta_{\tau,j})] + e^{-i\sqrt{2}(\varphi_{c,i}-\varphi_{c,j})} \cos[\sqrt{2}(\varphi_{\tau,i}-\varphi_{\tau,j})] \right\} \\
&\rightarrow - \sum_{i \neq j} \int dr t_{\perp,|i-j|}^2 e^{-i\sqrt{2}(\vartheta_{c,i}-\vartheta_{c,j})} \left\{ \cos[\sqrt{2}\vartheta_{\tau,i}] \cos[\sqrt{2}\vartheta_{\tau,j}] + \sin[\sqrt{2}\vartheta_{\tau,i}] \sin[\sqrt{2}\vartheta_{\tau,j}] \right\}, \tag{D15}
\end{aligned}$$

$$\begin{aligned}
T_{\text{SDW}} &= - \sum_{i \neq j} \int dr t_{\perp,|i-j|}^2 \left\{ e^{-i(\vartheta_{1,i}-\varphi_{1,i})} e^{i(\vartheta_{1,j}-\varphi_{1,j})} [e^{-i(\vartheta_{2,i}+\varphi_{2,i})} e^{i(\vartheta_{2,j}+\varphi_{2,j})} + e^{-i(\vartheta_{2,j}+\varphi_{2,j})} e^{i(\vartheta_{2,i}+\varphi_{2,i})}] + (1 \leftrightarrow 2) \right\} \\
&= - \sum_{i \neq j} \int dr t_{\perp,|i-j|}^2 \left\{ e^{-i\sqrt{2}(\vartheta_{c,i}-\vartheta_{c,j})} e^{i\sqrt{2}(\varphi_{\tau,i}-\varphi_{\tau,j})} + e^{i\sqrt{2}(\varphi_{c,i}-\varphi_{c,j})} e^{-i\sqrt{2}(\vartheta_{\tau,i}-\vartheta_{\tau,j})} + (\varphi_{\tau}, \vartheta_{\tau} \leftrightarrow -\varphi_{\tau}, -\vartheta_{\tau}) \right\} \\
&\rightarrow - \sum_{i \neq j} \int dr t_{\perp,|i-j|}^2 e^{i\sqrt{2}(\varphi_{c,i}-\varphi_{c,j})} \cos[\sqrt{2}(\vartheta_{\tau,i}-\vartheta_{\tau,j})] \\
&= - \sum_{i \neq j} \int dr t_{\perp,|i-j|}^2 e^{i\sqrt{2}(\varphi_{c,i}-\varphi_{c,j})} \left\{ \cos[\sqrt{2}\vartheta_{\tau,i}] \cos[\sqrt{2}\vartheta_{\tau,j}] + \sin[\sqrt{2}\vartheta_{\tau,i}] \sin[\sqrt{2}\vartheta_{\tau,j}] \right\}, \tag{D16}
\end{aligned}$$

where we only keep the relevant terms upon pinning the ϑ_{τ} field.

According to Eqs. (D15) and (D16), T_{SC} and T_{SDW} contribute to the (π) -SC and (π) -SDW channels of the two-body inter-edge tunneling, respectively. These contributions are reflected in the RG flow equations, which incorporate terms of order $\mathcal{O}(t_{\perp}^2)$:

$$\frac{d\tilde{J}_{\text{SC},N}}{dl} = (2 - \eta_{\text{SC},N})\tilde{J}_{\text{SC},N} + \mathcal{O}(t_{\perp,N}^2), \tag{D17}$$

$$\frac{d\tilde{J}_{\text{SDW},N}}{dl} = (2 - \eta_{\text{SDW},N})\tilde{J}_{\text{SDW},N} + \mathcal{O}(t_{\perp,N}^2). \tag{D18}$$

As indicated by Eqs. (D15) and (D16), although $\tilde{J}_{\text{SC},N}(l=0)$ and $\tilde{J}_{\text{SDW},N}(l=0)$ vanish at the bare level, nonzero values for $\tilde{J}_{\text{SC},N}$ and $\tilde{J}_{\text{SDW},N}$ are generated during the RG flow due to finite $t_{\perp,N}(l=0)$ [23]. These RG equations thus provide leading-order estimates of $\tilde{J}_{\text{SC},N}(l \rightarrow 0)$ and $\tilde{J}_{\text{SDW},N}(l \rightarrow 0)$, which are used to calculate the characteristic length L^* and temperature T^* , as discussed in the main text.

-
- [1] J. Chang, E. Blackburn, A. T. Holmes, N. B. Christensen, J. Larsen, J. Mesot, R. Liang, D. A. Bonn, W. N. Hardy, A. Watenphul, M. v. Zimmermann, E. M. Forgan, and S. M. Hayden, Direct observation of competition between superconductivity and charge density wave order in $\text{YBa}_2\text{Cu}_3\text{O}_{6.67}$, *Nature Physics* **8**, 871 (2012).
- [2] E. Fradkin, S. A. Kivelson, and J. M. Tranquada, Colloquium: Theory of intertwined orders in high temperature superconductors, *Rev. Mod. Phys.* **87**, 457 (2015).
- [3] M. Kang, S. Fang, J. Yoo, B. R. Ortiz, Y. M. Oey, J. Choi, S. H. Ryu, J. Kim, C. Jozwiak, A. Bostwick, E. Rotenberg, E. Kaxiras, J. G. Checkelsky, S. D. Wilson, J.-H. Park, and R. Comin, Charge order landscape and competition with superconductivity in kagome metals, *Nature Materials* **22**, 186 (2023).
- [4] F. H. Yu, D. H. Ma, W. Z. Zhuo, S. Q. Liu, X. K. Wen, B. Lei, J. J. Ying, and X. H. Chen, Unusual competition of superconductivity and charge-density-wave state in a compressed topological kagome metal, *Nature Commun-*
- nications* **12**, 3645 (2021).
- [5] S. D. Wilson and B. R. Ortiz, Av3sb5 kagome superconductors, *Nature Reviews Materials* **9**, 420 (2024).
- [6] B. Song, T. Ying, X. Wu, W. Xia, Q. Yin, Q. Zhang, Y. Song, X. Yang, J. Guo, L. Gu, X. Chen, J. Hu, A. P. Schnyder, H. Lei, Y. Guo, and S. Li, Anomalous enhancement of charge density wave in kagome superconductor CsV_3Sb_5 approaching the 2d limit, *Nature Communications* **14**, 2492 (2023).
- [7] N. N. Wang, K. Y. Chen, Q. W. Yin, Y. N. N. Ma, B. Y. Pan, X. Yang, X. Y. Ji, S. L. Wu, P. F. Shan, S. X. Xu, Z. J. Tu, C. S. Gong, G. T. Liu, G. Li, Y. Uwatoko, X. L. Dong, H. C. Lei, J. P. Sun, and J.-G. Cheng, Competition between charge-density-wave and superconductivity in the kagome metal RbV_3Sb_5 , *Phys. Rev. Res.* **3**, 043018 (2021).
- [8] Y. Song, T. Ying, X. Chen, X. Han, X. Wu, A. P. Schnyder, Y. Huang, J.-g. Guo, and X. Chen, Competition of superconductivity and charge density wave in selec-

- tive oxidized csv_3sb_5 thin flakes, *Phys. Rev. Lett.* **127**, 237001 (2021).
- [9] H. Tan, Y. Liu, Z. Wang, and B. Yan, Charge density waves and electronic properties of superconducting kagome metals, *Phys. Rev. Lett.* **127**, 046401 (2021).
- [10] Q. Xiao, Y. Lin, Q. Li, X. Zheng, S. Francoual, C. Plueckthun, W. Xia, Q. Qiu, S. Zhang, Y. Guo, J. Feng, and Y. Peng, Coexistence of multiple stacking charge density waves in kagome superconductor csv_3sb_5 , *Phys. Rev. Res.* **5**, L012032 (2023).
- [11] P. Cai, X. Zhou, W. Ruan, A. Wang, X. Chen, D.-H. Lee, and Y. Wang, Visualizing the microscopic coexistence of spin density wave and superconductivity in underdoped nafel-coxas , *Nature Communications* **4**, 1596 (2013).
- [12] Q. Q. Ge, Z. R. Ye, M. Xu, Y. Zhang, J. Jiang, B. P. Xie, Y. Song, C. L. Zhang, P. Dai, and D. L. Feng, Anisotropic but nodeless superconducting gap in the presence of spin-density wave in iron-pnictide superconductor $\text{nafel}_{1-x}\text{coxAs}$, *Phys. Rev. X* **3**, 011020 (2013).
- [13] A. A. Kordyuk, Iron-based superconductors: Magnetism, superconductivity, and electronic structure (review article), *Low Temperature Physics* **38**, 888 (2012).
- [14] R. Khasanov, T. J. Hicken, D. J. Gawryluk, V. Sazgari, I. Plokhikh, L. P. Sorel, M. Bartkowiak, S. Bötzel, F. Lechermann, I. M. Eremin, H. Luetkens, and Z. Guguchia, Pressure-enhanced splitting of density wave transitions in la3ni2o7-\delta , *Nature Physics* **21**, 430 (2025).
- [15] C. Lane, R. Zhang, B. Barbiellini, R. S. Markiewicz, A. Bansil, J. Sun, and J.-X. Zhu, Competing incommensurate spin fluctuations and magnetic excitations in infinite-layer nickelate superconductors, *Communications Physics* **6**, 90 (2023).
- [16] L. J. Azevedo, J. E. Schirber, J. M. Williams, M. A. Beno, and D. R. Stephens, Competition between superconductivity and spin-density waves in an organic conductor, bis-tetramethyltetraselenafulvalenium hexafluorophosphate, *Phys. Rev. B* **30**, 1570 (1984).
- [17] T. Vuletić, P. Auban-Senzier, C. Pasquier, S. Tomić, D. Jérôme, M. Héritier, and K. Bechgaard, Coexistence of superconductivity and spin density wave orderings in the organic superconductor $(\text{tmtsf})_2\text{pf}_6$, *The European Physical Journal B - Condensed Matter and Complex Systems* **25**, 319 (2002).
- [18] Y. Cao, D. Rodan-Legrain, J. M. Park, N. F. Q. Yuan, K. Watanabe, T. Taniguchi, R. M. Fernandes, L. Fu, and P. Jarillo-Herrero, Nematicity and competing orders in superconducting magic-angle graphene, *Science* **372**, 264 (2021).
- [19] R. Soto-Garrido, G. Y. Cho, and E. Fradkin, Quasi-one-dimensional pair density wave superconducting state, *Phys. Rev. B* **91**, 195102 (2015).
- [20] A. V. Rozhkov, Superconductivity without attraction in a quasi-one-dimensional metal, *Phys. Rev. B* **79**, 224520 (2009).
- [21] R. Duprat and C. Bourbonnais, Interplay between spin-density-wave and superconducting states in quasi-one-dimensional conductors, *The European Physical Journal B - Condensed Matter and Complex Systems* **21**, 219 (2001).
- [22] M. E. Palistrant and I. V. Pédure, Coexistence of spin-density wave and superconductivity in quasi-one-dimensional systems, *Theoretical and Mathematical Physics* **62**, 78 (1985).
- [23] T. Giamarchi, *Quantum Physics in One Dimension* (Oxford University Press, New York, 2003).
- [24] Y.-M. Xie and N. Nagaosa, *Quasi-one-dimensional superconductors in luther-emery liquids* (2025), arXiv:2501.02185 [cond-mat.str-el].
- [25] T. Senthil and M. P. A. Fisher, Competing orders, nonlinear sigma models, and topological terms in quantum magnets, *Phys. Rev. B* **74**, 064405 (2006).
- [26] K. K. W. Ma, O. b. u. Türker, A. Seidel, and K. Yang, Competing phases and intertwined orders in coupled wires near the self-dual point, *Phys. Rev. B* **108**, 245138 (2023).
- [27] A. Georges, T. Giamarchi, and N. Sandler, Interchain conductivity of coupled luttinger liquids and organic conductors, *Phys. Rev. B* **61**, 16393 (2000).
- [28] B. Wang, Y.-C. Hung, X. Zhou, A. Bansil, and H. Lin, Higher-order topological phases hidden in quantum spin hall insulators, *Phys. Rev. B* **108**, 245103 (2023).
- [29] J. Henke, M. Kurttutan, J. Kruthoff, and J. van Wezel, Topological invariants of rotationally symmetric crystals, *Phys. Rev. B* **104**, L201110 (2021).
- [30] L. Liu, Y. Liu, J. Li, H. Wu, and Q. Liu, Orbital doublet driven even-spin chern insulators, *Phys. Rev. B* **110**, 035161 (2024).
- [31] Y.-C. Hung, B. Wang, C.-H. Hsu, A. Bansil, and H. Lin, Time-reversal soliton pairs in even spin chern number higher-order topological insulators, *Phys. Rev. B* **110**, 035125 (2024).
- [32] Y.-C. Hung, C.-H. Hsu, and A. Bansil, Majorana kramers pairs in synthetic high-spin chern insulators, *Phys. Rev. B* **111**, 245145 (2025).
- [33] E. Prodan, Robustness of the spin-chern number, *Phys. Rev. B* **80**, 125327 (2009).
- [34] H. Shulman and E. Prodan, Robust extended states in a topological bulk model with even spin-chern invariant (2010), arXiv:1011.5456 [cond-mat.dis-nn].
- [35] B. Wang, Y.-C. Hung, X. Zhou, T. Ong, and H. Lin, Feature spectrum topology (2023), arXiv:2310.14832 [cond-mat.mtrl-sci].
- [36] K.-S. Lin, G. Palumbo, Z. Guo, Y. Hwang, J. Blackburn, D. P. Shoemaker, F. Mahmood, Z. Wang, G. A. Fiete, B. J. Wieder, and B. Bradlyn, Spin-resolved topology and partial axion angles in three-dimensional insulators, *Nature Communications* **15**, 550 (2024).
- [37] L. Fu, Topological crystalline insulators, *Phys. Rev. Lett.* **106**, 106802 (2011).
- [38] Y.-T. Yao, X. Zhou, Y.-C. Hung, H. Lin, A. Bansil, and T.-R. Chang, Feature-energy duality of topological boundary states in a multilayer quantum spin hall insulator, *Phys. Rev. B* **109**, 155143 (2024).
- [39] J. Lefevre, M. Kobayashi, G. Patriarche, N. Findling, D. Troadec, M. Ferrier, S. Guéron, H. Bouchiat, T. Sasagawa, and R. Deblock, *Quantum coherent transport of 1d ballistic states in second order topological insulator bi_4br_4* (2025), arXiv:2502.13837 [cond-mat.mes-hall].
- [40] B. Wang, X. Zhou, Y.-C. Hung, Y.-C. Lin, H. Lin, and A. Bansil, High spin-chern-number insulator in alpha-antimonene with a hidden topological phase, *2D Materials* **11**, 025033 (2024).
- [41] L. Liu, Y. Liu, J. Li, H. Wu, and Q. Liu, Quantum spin hall effect protected by spin $u(1)$ quasisymmetry, *Phys. Rev. B* **110**, L161104 (2024).
- [42] J. L. Lado, D. Guterding, P. Barone, R. Valentí, and V. Pardo, Quantum spin hall effect in rutile-based oxide

- multilayers, *Phys. Rev. B* **94**, 235111 (2016).
- [43] K. Kang, B. Shen, Y. Qiu, Y. Zeng, Z. Xia, K. Watanabe, T. Taniguchi, J. Shan, and K. F. Mak, Evidence of the fractional quantum spin Hall effect in moiré MoTe₂, *Nature* **628**, 522 (2024).
- [44] K. Kang, Y. Qiu, K. Watanabe, T. Taniguchi, J. Shan, and K. F. Mak, Double quantum spin hall phase in moiré wse₂, *Nano Letters* **24**, 14901 (2024).
- [45] W. H. Campos, P. H. Penteado, J. Zanon, P. E. Faria Junior, D. R. Candido, and J. C. Egues, Dual topological insulator with mirror symmetry protected helical edge states, *Phys. Rev. B* **110**, 195142 (2024).
- [46] P. Dziawa, B. J. Kowalski, K. Dybko, R. Buczko, A. Szczerbakow, M. Szot, E. Lusakowska, T. Balasubramanian, B. M. Wojek, M. H. Berntsen, O. Tjernberg, and T. Story, Topological crystalline insulator states in pb_{1-x}sn_xse, *Nature Materials* **11**, 1023 (2012).
- [47] Y. Tanaka, Z. Ren, T. Sato, K. Nakayama, S. Souma, T. Takahashi, K. Segawa, and Y. Ando, Experimental realization of a topological crystalline insulator in sn₂, *Nature Physics* **8**, 800 (2012).
- [48] J. Liu, T. H. Hsieh, P. Wei, W. Duan, J. Moodera, and L. Fu, Spin-filtered edge states with an electrically tunable gap in a two-dimensional topological crystalline insulator, *Nature Materials* **13**, 178 (2014).
- [49] J. Liu, X. Qian, and L. Fu, Crystal field effect induced topological crystalline insulators in monolayer iv–vi semiconductors, *Nano Letters* **15**, 2657 (2015).
- [50] A. Luther and V. J. Emery, Backward scattering in the one-dimensional electron gas, *Phys. Rev. Lett.* **33**, 589 (1974).
- [51] See, e.g., Ref. [52] for a review of various relevant backscattering mechanisms.
- [52] C.-H. Hsu, P. Stano, J. Klinovaja, and D. Loss, Helical liquids in semiconductors, *Semiconductor Science and Technology* **36**, 123003 (2021).
- [53] A. Vishwanath and D. Carpentier, Two-dimensional anisotropic non-fermi-liquid phase of coupled luttinger liquids, *Phys. Rev. Lett.* **86**, 676 (2001).
- [54] V. J. Emery, E. Fradkin, S. A. Kivelson, and T. C. Lubensky, Quantum theory of the smectic metal state in stripe phases, *Phys. Rev. Lett.* **85**, 2160 (2000).
- [55] M. Thakurathi, P. Simon, I. Mandal, J. Klinovaja, and D. Loss, Majorana kramers pairs in rashba double nanowires with interactions and disorder, *Phys. Rev. B* **97**, 045415 (2018).
- [56] N. Mao, C. Xu, T. Bao, N. Peshcherenko, C. Felser, and Y. Zhang, *Universal giant spin hall effect in moire metal* (2025), [arXiv:2504.16179](https://arxiv.org/abs/2504.16179) [cond-mat.mes-hall].
- [57] P. Michetti, J. C. Budich, E. G. Novik, and P. Recher, Tunable quantum spin hall effect in double quantum wells, *Phys. Rev. B* **85**, 125309 (2012).
- [58] G. M. Gusev, E. B. Olshanetsky, F. G. G. Hernandez, O. E. Raichev, N. N. Mikhailov, and S. A. Dvoretzky, Two-dimensional topological insulator state in double hgte quantum well, *Phys. Rev. B* **101**, 241302 (2020).
- [59] Z.-R. Liu, L.-H. Hu, C.-Z. Chen, B. Zhou, and D.-H. Xu, Topological excitonic corner states and nodal phase in bilayer quantum spin hall insulators, *Phys. Rev. B* **103**, L201115 (2021).
- [60] R. A. Santos, D. B. Gutman, and S. T. Carr, Phase diagram of two interacting helical states, *Phys. Rev. B* **93**, 235436 (2016).
- [61] G. J. Ferreira, D. R. Candido, F. G. G. Hernandez, G. M. Gusev, E. B. Olshanetsky, N. N. Mikhailov, and S. A. Dvoretzky, Engineering topological phases in triple hgte/cdte quantum wells, *Scientific Reports* **12**, 2617 (2022).
- [62] S. S. Krishtopenko, W. Knap, and F. Tepe, Phase transitions in two tunnel-coupled hgte quantum wells: Bilayer graphene analogy and beyond, *Scientific Reports* **6**, 30755 (2016).
- [63] Z. Bi and L. Fu, Excitonic density wave and spin-valley superfluid in bilayer transition metal dichalcogenide, *Nature Communications* **12**, 642 (2021).
- [64] A. Laturia, M. L. Van de Put, and W. G. Vandenberghe, Dielectric properties of hexagonal boron nitride and transition metal dichalcogenides: from monolayer to bulk, *npj 2D Materials and Applications* **2**, 6 (2018).
- [65] Y.-C. Hung, Codes for reproducing figs. 4, 5, and 6., <https://github.com/lengentyh/Competing-orders-in-DQSHI> (2025).
- [66] C.-H. Hsu, P. Stano, J. Klinovaja, and D. Loss, Majorana kramers pairs in higher-order topological insulators, *Phys. Rev. Lett.* **121**, 196801 (2018).